Electrochimica Acta 279 (2018) 289–300

Contents lists available at ScienceDirect

Electrochimica Acta

journal homepage: www.elsevier.com/locate/electacta

A silica/carbon composite as anode for lithium-ion batteries with a large rate capability: Experiment and theoretical considerations

G. Lener [a, *], A.A. Garcia-Blanco [b], O. Furlong [b], M. Nazzarro [b], K. Sapag [b], D.E. Barraco [c], E.P.M. Leiva [a, **]

[a] INFIQC-Conicet, Facultad de Ciencias Químicas, Departamento de Química Teórica y Computacional, Universidad Nacional de Córdoba, Argentina
[b] INFAP-Conicet, Facultad de Ciencias Físico-Matemáticas, Universidad Nacional de San Luis, Argentina
[c] IFEG-Conicet, Facultad de Matemática Astronomía y Física, Universidad Nacional de Córdoba, Argentina

ARTICLE INFO

Article history:
Received 22 December 2017
Received in revised form
13 April 2018
Accepted 5 May 2018
Available online 8 May 2018

Keywords:
SiO_2/C
Mesoporous structures
Silica-carbon composite
High rate capability
Lithium-ion battery
Thermodynamic analysis

ABSTRACT

New generations of materials are necessary to provide practical and economical solutions for electrode fabrication in lithium ion batteries. To this end, in the present work we propose a negative electrode based on a SiO_2/C interconnected composite able to charge/discharge at high current regimes while maintaining a very good capacity. In order to have a better understanding of the phenomena that occur in the charge/discharge process, we combined experimental techniques (XPS, DRX, EIS, etc.) with theoretical calculations based on DFT to obtain the thermodynamics of the formation of the reaction products as a function of the cell potential. These results were combined with our experiments and results from the literature to demonstrate the different reactions that could occur. The present material provides a superior performance compared with analogous materials from the literature and may thus be an important tool for obtaining practical solutions in both stationary and mobile electrical devices.

1. Introduction

Lithium-ion batteries (LIBs) represent a major advance in the storage of renewable energy because they allow energy to be stored with large efficiency and power, which can be used when required. Currently LIBs batteries are utilized for electronic devices, electric vehicles, and for energy storage from various renewable resources, such as photovoltaics and wind, among others. Moreover, energy may be stored and become available as demand varies.

Current research is often focused on obtaining high capacity anodes based on silicon, due to its large theoretical capacity of 3579 mAh g^{-1} being significantly higher than that of graphite (372 mAh g^{-1}), which is usually used in anodes [1]. However, it is well known that silicon undergoes a huge expansion process, which provokes the pulverization and disconnection of the electric contact, with the electrode losing most of its capacity in the first cycles [2]. In fact, anodes based on metallic silicon suffer a 300% expansion, due to alloy formation (Li_xSi_y), while graphite dilates only 7% as a consequence of the intercalation mechanism of Li^+ into graphite layers [3]. In the former, the negative effect of expansion has been partially resolved by using different strategies, as described in extensive reviews from the literature [2–6]. To prevent particle fracture, some of these strategies include the use of including Si nanoparticles, Si nanowires, nanotubes, Si thin flakes, Si nanopillars, Si nanospheres, nanostructured spheres, combinations of nanoparticles and nanowires [2]. In other approaches, Si nanoparticles are coated, encapsulated, or nanodispersed, in hybrid Si/C nanostructures, to avoid direct contact with the electrolyte [6]. Thin films and alloys with different active elements (H, Mg, Ca, Ag, Zn, B, Al, C, Sn) have also been tested as alternatives [2]. A different approach has been that of using SiO and SiO_2 based electrodes. SiO_2 has been used as starting point to get Si based anodes by the reduction of SiO_2/C pre-synthesized composites using magnesiothermic reduction [7,8]. Nevertheless, the main drawback of these synthesis strategies resides in the high cost of these processes, as both involve at some stage SiO_2 reduction to silicon, which is a highly activated and therefore expensive procedure [9]. The volumetric expansion of silicon particles is a bigger problem at the industrial scale [10], and in addition, it is necessary to improve the

* Corresponding author.
** Corresponding author.
E-mail addresses: germanlener@gmail.com (G. Lener), eze_leiva@yahoo.com.ar (E.P.M. Leiva).

https://doi.org/10.1016/j.electacta.2018.05.050
0013-4686/

reversible charge/discharge capacity to achieve a good ionic conductivity for the processes involving Li^+ migration. In this sense, it is important to enhance the ionic and electronic conductivity of the electrode materials to maintain the specific capacity at high current densities. Materials based on SiO_2 represent an appealing alternative to develop silicon based anodes, due to the fact that silica is one of the most abundant components of the earth crust, with several clays having complex porous nanostructures of SiO_2. The synthesis of SiO_2nanoporous material is generally straightforward and cheap.

According to the literature, the electrochemical reactions that may take place during the lithiation of SiO_2 can be summarized as [9]:

$$R1-) \quad 4Li^+ + 4e^- + 5SiO_2 \leftrightarrow 2Li_2Si_2O_5 + Si$$

$$R2-) \quad 4Li^+ + 4e^- + 3SiO_2 \rightarrow 2Li_2SiO_3 + 2Si$$

$$R3-) \quad 4Li^+ + 4e^- + 2SiO_2 \rightarrow Li_4SiO_4 + Si$$

$$R4-) \quad 4Li^+ + 4e^- + SiO_2 \rightarrow 2Li_2O + Si$$

The previous reactions, those not involving the formation of Li-Si alloys, will be globally denominated here as step 1, and the subsequent lithiation of Si after step 1 will be denominated as step 2, according to the following reaction:

$$R5-) \quad 15Li^+ + 15e^- + 4Si \rightarrow Li_{15}Si_4$$

where we have used the stoichiometry proposed by Obrovac et al. [11].

Theoretical electrode capacities for step 1 were calculated by taking into account reactions R1, R2, R3 and R4, and are reported in the second column of Table 1. The capacity due to the further lithium storage in the Si material arising from these reactions (step 2) was calculated assuming the formation of $Li_{15}Si_4$, and is reported in the third column of Table 1. Column 4 shows the sum of the capacities reported in columns 2 and 3, so this represents the total capacity attainable by step 1 followed by step 2. In principle, reaction R4 followed by the lithiation of the generated Si promises a very large capacity (3462 mAh g^{-1}). However, to make a realistic estimation, it must be taken into account that only reaction R1, involving $Li_2Si_2O_5$, has been found to perform reversibly upon SiO_2 lithiation [12–15], and involves the coexistence of reaction R1 with the lithiation of the Si metal. Thus, the results in the fourth column are only applicable, according to the results from the literature, for reaction R1, because the other capacities can only be obtained if reactions R2-R4 are made reversible, something that has not been observed so far. It should be emphasized that all the theoretical specific capacities are larger than that of graphite (372 mAh g^{-1}) (Table 1).

In the general case, where the different reactions shown above may occur, the capacity would depend on the relative quantities of the inactive phases formed in the reaction. In this way, the capacity measured experimentally will depend on the relative contributions of the different reactions, whose relative weight may present thermodynamic or kinetic control.

The main problem of silica is its electric insulating behavior. As the conduction of electrons is not possible in pure SiO_2, this limits the possibility of obtaining silicon and the co-products of the reactions R1-R4 from SiO_2. In Fact, this path of reaction is still one of the most important processes, because it forms Si, which can be subsequently lithiated to yield Li_xSi_y. Moreover, Lithium oxide/silicates play an important role in providing ionic conductivity, buffering the volume expansion during the charge/discharge process and allowing the generation of a stable SEI [16–20]. Thus, to obtain a good electrochemical response from silica, it is necessary to improve its electrical conductivity. One way to increase the electronic conductivity of SiO_2 is to synthesize a hybrid composite SiO_2/C, where the carbon phase provides a conductive path of electrons to ensure the conversion of SiO_2 to Si and co-products. An example of this approach can be found in the work of Li et al., where in order to achieve the reduction of silica and obtain a charge/discharge process porous SiO_2/C nanoparticles were synthesized, which resulted in an excellent performance as anode for LIBs [21]. These authors showed that the hard carbon formed in the composite facilitates the ionic and electronic conduction, thereby improving the kinetic migration of species in the materials and consequently enhancing the charge/discharge profile and rate capability [21–25]. A detailed analysis of the literature reporting other approaches to prepare SiO_2/C composites is given in Section 4.6, in the context of the present work.

On the basis of the discussion above, the aim of the present work was to generate a composite based on a highly ordered SiO_2 that included a hard carbon structure to improve the electronic and ionic conductivity, thus avoiding the use of an expensive, complicated, and long path synthesis of active materials. Of the several types of mesoporous SiO_2 materials that could be utilized, in current investigation we used SBA-15 as the template material as it has a spatial arrangement of two domains of pores: one with a pore diameter of 6–8 nm, and the other with a pore diameter of about 2 nm or less, creating a combination of mesopores interconnected with micropores. If the pores are filled with the hard carbon conductor, the electronic and ionic conduction can be improved [22], generating a conductive skeleton to enhance SiO_2 conversion into silicon and co-products. As described above, the advantage of this material resides in the fact that the co-products are active too, thus mitigating volume expansion in the lithiation and improving the ion diffusion of Li^+.

The carbon formed in the SBA-15 pores is the so-called CMK-3, whose properties as a supercapacitor are well known, which presents a reversible charge/discharge behavior when used as anode in lithium ion-batteries [26]. To study the role of each component of the composite, we compared the electrochemical performance of the SBA-15, CMK-3 and SBA-15/C composites, and to analyze the occurrence of the different species that may arise during the charge/discharge process, we carried out ab-initio calculations to obtain the free energies of SiO_2lithiation according to the reactions R1-R4 reported in a previous work [9].

Table 1
Theoretical capacities for Li-ion storage. Column 2 gives the theoretical electrode capacities for Li^+ storage according to the reactions R1, R2, R3 and R4 given in the text. Column 3 gives the additional Li^+ storage capacity due to the formation of the alloy $Li_{15}Si_4$ from the Si material resulting from reactions R1-R4. Column 4 is the sum of the capacities reported in columns 2 and 3.

Reaction	Theoretical Capacity (mAh g^{-1}) Step 1	Theoretical Capacity (mAh g^{-1}) Step 2	Total Theoretical Capacity (mAh g^{-1}) Step1 + Step 2
R1	357	335	692
R2	595	558	1153
R3	893	837	1720
R4	1787	1675	3462

In the present work, we extended the analysis of the Gibbs free energy of the lithiation phenomenon as a function of the cell potential. To the best of our knowledge, this is the first time that the present types of experimental studies have been performed for the SBA-15 and SBA-15/C compounds and combined with theoretical calculations to yield a complete picture of the present phenomenon.

2. Experimental

2.1. Material preparation

The SBA-15 support was synthesized according to the methodology described by Zhao et al. [27,28] using Pluronictriblock copolymer P123 (EO20-PO70-EO20) as organic structure-directing agent and tetraethyl orthosilicate (TEOS) as silica source. Thus, 12 g of Pluronic P123 were dissolved in 360 ml of water and 60 ml of HCl solution (37%, w/w) with stirring at 313 K for 3 h. Then, 27 ml of TEOS were added, and the solution was kept stirring at 313 K for 24 h. The mixture was aged at 363 K overnight, without stirring. The solid was recovered by filtration, washed, and dried in air at room temperature (RT). Calcination in air was carried out from room temperature up to 773 K at a rate of 1 K/min, holding the latter temperature for 6 h.

The SiO_2/C composite was synthesized by impregnation, using sucrose as carbon source. Thus, 2 g of sucrose were dissolved per gram of SBA-15. The mixture sucrose/SBA-15 was stirred during 2 h and 0.14 g of H_2SO_4were added. Then, the solution was stirred one more hour. The sample was dried at 80 °C during 6 h. The heat treatment was carried out using N_2 as inert gas, heating at 700 °C, per 5 h. The resulting solid was divided into two samples for different final treatments: one was heated at 900 °C in N_2 for 5 h to get the final SiO_2/C composite. The other one was treated with NaOH 1 M at 60 °C for 2 h to etch the SBA-15 structure and get the mesoporous CMK-3 carbon. Finally CMK-3 was heated at 900 °C for 5 h in Ar atmosphere. As it is known, the final temperature is important to desorb the functional groups; in the case of SBA-15/C composite, the desorption of siloxane surface groups may occur in the pyrolized treatment at high temperatures. In the case of carbon CMK-3 the temperature allows the desorption of functional groups from the surface, yielding structures suitable for electronic conduction [29]. Pioneering work using high temperature pyrolysis to obtain Si-O composites with lithium-storage capability was undertaken by Wilson et al. [30].

2.2. Material characterization

The adsorption-desorption isotherms of N_2 at −221 °C were measured in a Micromeritics ASAP 2000 equipment. The samples were previously outgassed at 250 °C for 12 h. Textural properties, such as the specific surface area (S_{BET}) and micropore volume ($V_{\mu p}$) were calculated from the experimental data, see Table ST1. The pore size distribution (PSD) was calculated by fitting experimental adsorption data to NLDFT kernels of cylindrical pore geometry for silica or carbon materials [31]. The X-ray diffraction patterns were recorded in a Shimadzu equipment, XD3A model, using Cu Kα radiation generated at 40 kV and 40 mA in the range $2\theta = 0.5–9°$ with steps of 0.02° and counting time of 2 s/step.

The pore wall thickness (b_d) of SBA-15 was calculated using N_2 adsorption and DRX data, as reported by Kruk et al. [32].

Thermogravimetric analyses (TGA) of approximately 5 mg of each compound were recorded on a TGA Q600 (TA Instruments) under air atmosphere, by equilibrating at 100 °C, and following a heating ramp rate of 10 °C min^{-1} up to 1300 °C.

X-ray photoelectron spectra of the samples were collected using a VG Microtech ESCA spectrometer with a non-monochromatic Al Kα radiation source (300 W, 15 kV, $h\nu = 1486.6$ eV), combined with a VG-100-AX hemispherical analyzer operating at 25 eV pass energy. The instrumental resolution was 0.1 eV. All the XPS spectra were calibrated with a reference to the adventitious C1s peak at 284.8 eV, to rule out any possible spectral shift due to a charging effect. The chamber pressure was kept at $<10^{-9}$ Torr during the measurements.

To remove the SEI after the cycling for XPS analysis, the samples were sputtered during a total time of 30 min with Ar^+ at an ion energy of 1.5 kV, and a sample current of 4 μA.

2.3. Electrochemical measurements

The electrochemical experiments with the anode materials were carried out using Autolab and Arbin potenciostats/galvanostats. A typical T-type cell was used with a disc of 8 mm of metallic lithium as the counter electrode and as the reference electrode. The working electrode was prepared with active materials, PVDF as the binder, and super-P carbon as conductive material at 80:10:10 ratios. N-methylpyrrolidone was used as solvent, of which 700 μl was added per 100 mg of active material. The mixture was deposited on a copper foil and dried at 80 °C overnight.

3. Theoretical calculations

In a previous work [9], we used the phonon calculation implemented in the quantum-espresso package [33] to determine the free energies required for the lithiation of SiO_2 to obtain the different materials reported in reactions (R1-R4). To analyze the relative stabilities of the previous materials at different potentials, it is useful to rewrite the previous equations as:

$$R6-)\quad \frac{4}{5}Li^+ + \frac{4}{5}e^- + SiO_2 \leftrightarrow \frac{2}{5}Li_2Si_2O_5 + \frac{1}{5}Si$$

$$R7-)\quad \frac{4}{3}Li^+ + \frac{4}{3}e^- + SiO_2 \rightarrow \frac{2}{3}Li_2SiO_3 + \frac{1}{3}Si$$

$$R8-)\quad 2Li^+ + 2e^- + SiO_2 \rightarrow \frac{1}{2}Li_4SiO_4 + \frac{1}{2}Si$$

$$R9-)\quad 4Li^+ + 4e^- + SiO_2 \rightarrow 2Li_2O + Si$$

The free energy change related to each of the previous equations gives the necessary spontaneity criterion for the reaction of a mol of SiO_2 with different amounts n_{Li^+} of Li^+ ions in solution and n_e electrons in the working electrode to yield different lithiated oxide species, say P_i with the stochiometric coefficient n_i. As a result of the reactions R6-R9, pure Si appears, with the stoichiometric number n_{Si}. Using this notation, the free energy for any of the reactions R6-R9 can be written as:

$$\Delta G_i = n_i\mu_i + n_{Si}\mu_{Si} - \mu_{SiO_2} - n_{Li^+}\tilde{\mu}^s_{Li^+} - n_e\tilde{\mu}^W_e \qquad (1)$$

where μ and $\tilde{\mu}$ denote the chemical and electrochemical potentials respectively. Thus, $\tilde{\mu}^W_e$ represents the electrochemical potential of electrons in the working electrode and $\tilde{\mu}^s_{Li^+}$ the electrochemical potential of Li^+ ions in solution. The last two terms are introduced in equation (1) because electrons and Li^+ ions may flow into and outside the material being lithiated.

Assuming that the electrode potential is measured with respect to a pure Li reference electrode immersed in the same solution as the working electrode, taking into account that $n_{Li^+} = n_e$ and substracting and adding a term $n_e\mu_{Li^0}$ (with μ_{Li^0} representing the

chemical potential of Li atoms in the pure lithium metal), we arrive to:

$$\Delta G_i = n_i\mu_i + n_{Si}\mu_{Si} - \mu_{SiO_2} - n_e\mu_{Li^0} + n_e\tilde{\mu}_e^R + n_{Li^+}\tilde{\mu}_{Li^+}^R - n_{Li^+}\tilde{\mu}_{Li^+}^S - n_e\tilde{\mu}_e^W \quad (2)$$

where we have used the fact that for the reference Li electrode $\mu_{Li^0} = \tilde{\mu}_e^R + \tilde{\mu}_{Li^+}^R$, where $\tilde{\mu}_e^R$ and $\tilde{\mu}_{Li^+}^R$ are the electrochemical potentials of electrons and core ions in the reference electrode respectively. Since the Li^+ ion are free to flow between working and reference electrode, we have $\tilde{\mu}_{Li^+}^R = \tilde{\mu}_{Li^+}^S$ so that the previous equation simplifies to:

$$\Delta G_i = n_i\mu_i + n_{Si}\mu_{Si} - \mu_{SiO_2} - n_e\mu_{Li^0} + n_e\left(\tilde{\mu}_e^R - \tilde{\mu}_e^W\right) \quad (3)$$

And taking into account that cell potential V_{cell} measured with respect to the metallic lithium electrode is $V_{cell} = -(\tilde{\mu}_e^W - \tilde{\mu}_e^R)/e_0$, where e_0 is the elemental charge, we arrive at:

$$\Delta G_i = n_i\mu_i + n_{Si}\mu_{Si} - \mu_{SiO_2} - n_e\mu_{Li^0} + e_0 n_e V_{cell} \quad (4)$$

Equation (4) allows the stability of SiO_2 to be predicted at different electrode potentials, indicating its capability to yield the different products written in reactions R6-R9, once the chemical potentials of the different species are known. This is discussed below.

4. Results and discussion

4.1. Characterization

The ordered mesoporous materials were characterized by nitrogen adsorption and low angle X-ray diffraction (Fig. S1a–c), with the samples revealing the textural and structural features of SBA-15 and CMK-3. The analysis of the N_2 adsorption isotherm shows a PSD with a pore size of about 8 nm for mesopores and around 2 nm for micropores in SBA-15. On the other hand the pore size for CMK-3 was found to be around 5 nm for mesopores and about 1 nm for micropores.

The small-angle DRX in Fig. S1–c shows the characteristic reflections due to the hexagonal arrangement of the pore system of the SBA-15 [28]. The three peaks observed correspond to the 100, 110, and 200 reflections associated with the *p6mm* hexagonal symmetry, with the corresponding *d-spacings* being 10, 6 and 5 nm respectively, in good agreement with the values reported for the SBA-15 materials [28].

Fig. S1–d shows the thermogravimetric analysis in air of SBA-15/C, indicating that the composite presents a 45% C content. The combustion temperature of this carbon was about 600 °C, indicating a hard structured carbon.

Fig. S2 displays SEM micrographs for the nanostructures of SBA-15/C and CMK-3 synthesized in the present work. The SEM images shown in the figure were taken without any metallization, and as it was possible to use a large magnification, this indicated the electronic conductor character of these samples. The SBA-15/C composite shows a periodic interlayer of SiO_2/C with a separation of a few nanometers. As CMK-3 is the exact reverse replica of SBA-15, the typical nanoporous ordered structure can be observed in the SEM image.

Fig. 1 shows TEM micrographs for the nanostructures of SBA-15/C, SBA-15 and CMK-3, where the hexagonal geometry of the composites can be appreciated. Fig. 1a–b shows that the SBA-15/C composite maintains the ordered structure of SBA-15, so that the SiO_2 material is surrounded by carbon conductive structures that allow electron transfer for reactions R6-R9. Fig. 1e–f shows that the carbon structures remain ordered, dense and interconnected, even after SiO_2 dissolution. Fig. 1g show the STEM micrograph of SBA15-C and the correspondent EDS-STEM Fig. 1h show the distribution of the element in the composite.

4.2. Charge/discharge performance

In the following, we will refer to the lithiation/delithiation processes as charge/discharge processes respectively.

In this section, we present results for CMK-3, SBA-15 and SBA-15/C. In the first two cases, although we did not carry out a detailed study, these results are given so that by comparison the improved behavior of SBA-15/C can be observed. Thus, this demonstrates the synergistic effect noted between the underlying carbonaceous skeleton and the SiO_2 envelope of the SBA-15/C composite.

4.2.1. -SBA-15

The dQ/dV plot of the first charge cycle of the SBA-15 material (Fig. 2a) shows two high irreversible peaks in the first cycle at 1.5 and at 0.75 V, which may be attributed to the formation of products from irreversible reactions and SEI formation [9]. Fig. 2b shows the dQ/dV plot for the second cycle of charge/discharge of SBA-15, where a rather pseudo-capacitive behavior can be observed, with the insinuation of a couple of complementary shoulders in the potential region between 0.9 and 1.0 V. The charge/discharge performance is shown in Fig. 2c, revealing a rather poor reversible specific capacity. The charge and discharge profiles start to display similar values at the 5th cycle, with a yield of about 30 $mAhg^{-1}$, which drops to about 20 $mAhg^{-1}$at the 50th cycle. The reduction in the total amount of SiO_2 needed to obtain lithium silicates/oxide and silicon was probably kinetically inhibited due to the electrically insulating character of SiO_2 (the calculated band gap is 3.5 eV [34]).

4.2.2. -CMK-3

Fig. 3a shows the charge/discharge cycles for the CMK-3 anode. The first charge cycle presented a capacity of 3000 $mAhg^{-1}$ (not shown in the figure), which decreased to 446 mAh g^{-1} in the first discharge cycle, indicating a high irreversible capacity of 2554 mAh g^{-1}. The specific capacity decreases up to cycle 40, where it then stabilized at around of 250 mAh g^{-1}. The dQ/dV plot (Fig. 3b) of the first cycle shows two irreversible peaks at 0.9 V and 0.68 V respectively, and another peak at 0.1 V due to SEI formation and reduction of the functional groups with a high surface area of carbon [35]. However, these peaks were not present in the following cycles (Fig. 3c). It is worth noting that the apparent surface area obtained by the BET method was 1050 m^2g^{-1}, so that a large capacitive contribution would be expected due to the presence of large pores. At low potentials, an important negative value of dQ/dV is observed in Fig. 3c. According to the literature [36,37], Li^+ insertion into ordered porous carbon structures is expected at low potentials. However, a peak structure is not noted in the present case.

The exact mechanism of lithium storage in mesoporous ordered carbon has not been completely unraveled yet, due to its complexity and the fact that it involves different components such as connectivity, size distribution and pore shape, as well being affected by the nature of the electrolyte and the solid–liquid interface [38]. Also, Li^+ reversible insertion in CMK-3 at low potentials may occur in the defects in the primary and secondary porous structure of ordered carbon and at the graphite type interlayer site [22,29,36,38,39].

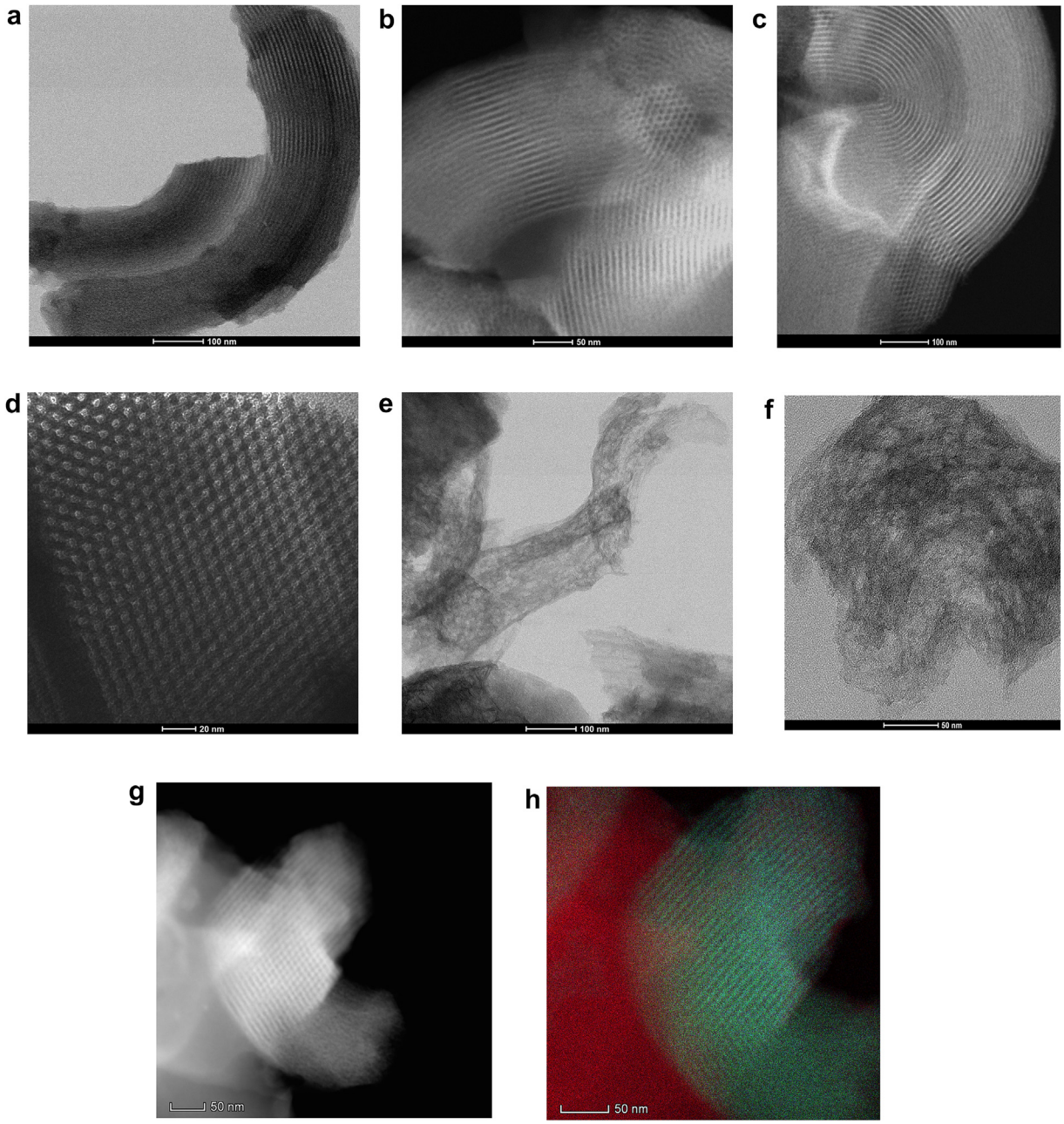

Fig. 1. TEM micrographs of SBA15, SBA15-C and CMK-3 at different magnifications. a-b-) SBA-15/C, c-d-) SBA-15, e-f-) CMK-3, g-) STEM of SBA15-C, h-) STEM-EDS for SBA15-C (green: Si, blue: O, red: C). (For interpretation of the references to colour in this figure legend, the reader is referred to the Web version of this article.)

4.2.3. SBA-15/C composite

As explained above, SBA-15/C is a 3D ordered silica mesoporous structure involving 8 nm diameter pores filled with carbon nanorods. These rods are in turn interconnected via smaller nanorods of carbon of 1 nm of diameter, which are surrounded by the SiO_2 template with wall thicknesses of about of 2 nm (see ST1). The presence of the ordered, conductive structure of CMK-3 carbon can permit the conduction of electrons into SBA-15, thereby improving the reduction of silica to silicon and facilitating the migration of ions and electrons to obtain Li_xSi_y structures.

Fig. 4a shows the galvanostatic charge/discharge profiles for the SBA-15/C composite from the 10th cycle onwards. It must be emphasized that the capacities shown refer to the weight of the SBA15/C composite. In the first cycle, the specific capacity is 1300 $mAhg^{-1}$ (not shown in the graph) upon charging and 480 mAh g^{-1} upon discharging, revealing an irreversible specific capacity of 820 mAh g^{-1}. From cycle 25 to cycle 80, the specific capacity remains at about 450 $mAhg^{-1}$, with a coulombic efficiency of 98%. From the cycle 80 to the cycle 300 the specific capacity remains at about 450 $mAhg^{-1}$ and the coulombic efficiency increase of 99.5%. The specific capacity then slightly decreases until cycle 25, probably due to remaining irreversible reactions with this decrease in capacity being concomitant with a relatively low coulombic efficiency. Then, as long as the latter approaches 100%, the specific capacity stabilizes. No appreciable changes in the morphologies of the particles are found after several charge/discharge cycles (See Fig. S3).

Fig. 4b shows the dQ/dV plot for cycles 1, 10 and 100. Irreversible

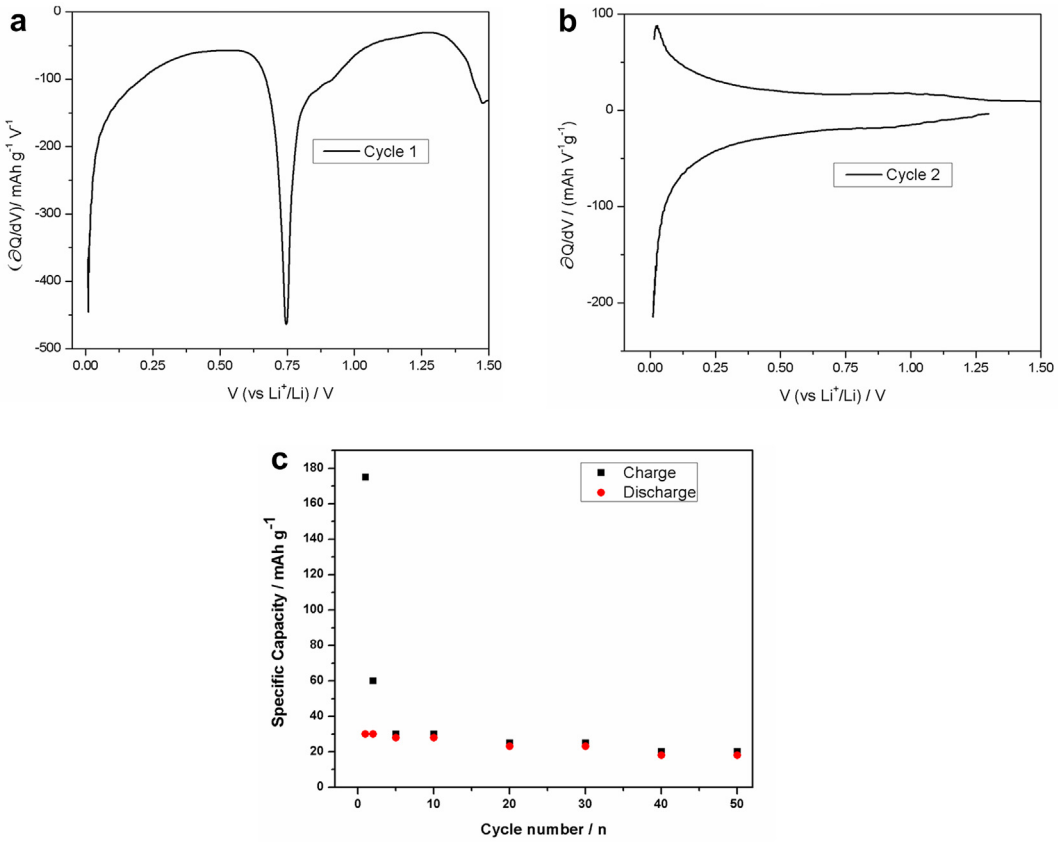

Fig. 2. a-) Differential charge capacity vs potential for the first cycle with SBA-15. Charged at 0.1 A g^{-1}. b-) Differential charge/discharge capacity vs potential for the 2nd cycle with SBA-15. Charged at 0.1 A g^{-1}. c-) Specific capacity vs number of cycles for SBA-15. Charged/discharged at 0.1 A g^{-1}.

peaks are found in the first cycle at 0.75 V and 0.1 V, which can be attributed to SEI formation as well as to the formation of Li_2O, $Li_2Si_2O_5$, Li_4SiO_4 and Si [9] (see below). After the early cycles, the cathodic curve shows reversible processes of lithiation, manifest in a peak at 0.43 V and two shoulders at 0.16 V and 0.04 V. The anodic curve has four well-defined reversible delithiation processes, with contributions at 0.045 V, 0.3 V, 0.47 V and 0.72 V, and the peaks becoming more evident with the cycling of the electrode.

On the basis of the bibliography referred to silica and silicon based electrodes, it can be concluded that two reversible lithiation/delithiation processes may take place: one involves the reversible lithiation of Si to get Li_xSi_y alloys [2,4,11,40] and another one involves the reversible lithiation of SiO_2 to get $Li_2Si_2O_5$ [14,15]. The typical cathodic peaks for Si lithiation occur at about 100 and 250 mV respectively, whereas anodic peaks can be observed at about 270 and 480 mV respectively [2,4,11,40]. Concerning the second type of processes, the lithiation of SiO_2 to form $Li_2Si_2O_5$ has been reported to take place below of 0.6 V in the cathodic curve [14]. In the dQ/dV plot shown in Fig. 4b, it can be found that for the present SiO_2/C composite, there is clear evidence in the cathodic profiles for a peak at 0.43 and some shoulders below 0.25 V. These features suggest that for the present composite the reversible contributions may be due to the lithiation of SiO_2 and Si.

4.3. XPS analysis

Fig. 5a shows the XPS spectra of the Si 2p of the electrode before any electrochemical treatment. The experimental peak is adequately fitted to the contribution of a single peak centered at 103.5 eV, which is the characteristic binding energy of Si in SiO_2 [8]. Fig. 5b shows the XPS spectra of the Si 2p of the discharged electrode after 30 cycles. The spectrum shown in Fig. 5b was obtained after sputtering with Ar^+ to remove the SEI. The broad band observed in this spectrum suggests the contribution of several peaks, hence the experimental results were fitted with excellent accordance to the spectra of Si 2p of SiO_2 (103.5 eV), Si 2p of Si-O in lithium silicates (102.2 eV) [12,13] and Si 2p of Si-C interaction (101.2 eV), indicating a complicated spectra with the coexistence of different reaction products [12].

From the relative contributions to the Si 2p spectrum in Fig. 5b, we can infer that a meaningful part of SiO_2 (37%) has been irreversibly converted to silicates, see Table ST2. On the other hand, it can also be inferred that an important part of silicon is in contact with the carbonaceous skeleton (22%). The remaining amount of silicon (41%) remains or is recovered as SiO_2. These values open the way to predict the capacity of Li storage in the present composite. If all the Si in contact with C (22%) were able to store lithium ions with the same capacity as that of pure Si, that is 3579 mAh g^{-1}, the contribution to the specific capacity of the silica composite would be 367 mAh g^{-1}, see supplementary information. On the other hand, assuming that all the SiO_2, which represent a 41% of the atomic percentage of Si, is able to store lithium by the reversible reaction R1, a contribution of 274 mAh g^{-1} to the total capacity is expected. Altogether, a total capacity of 641 mAh g^{-1} is expected for the present composite if the lithium storage mechanism involves reaction R1 and ion storage in Si emerging from the irreversible reactions R2-R4. These results are summarized in Table ST2 and described in the Supplementary information.

4.4. Rate capability experiments

For the rate capability experiment, two sets of measurements

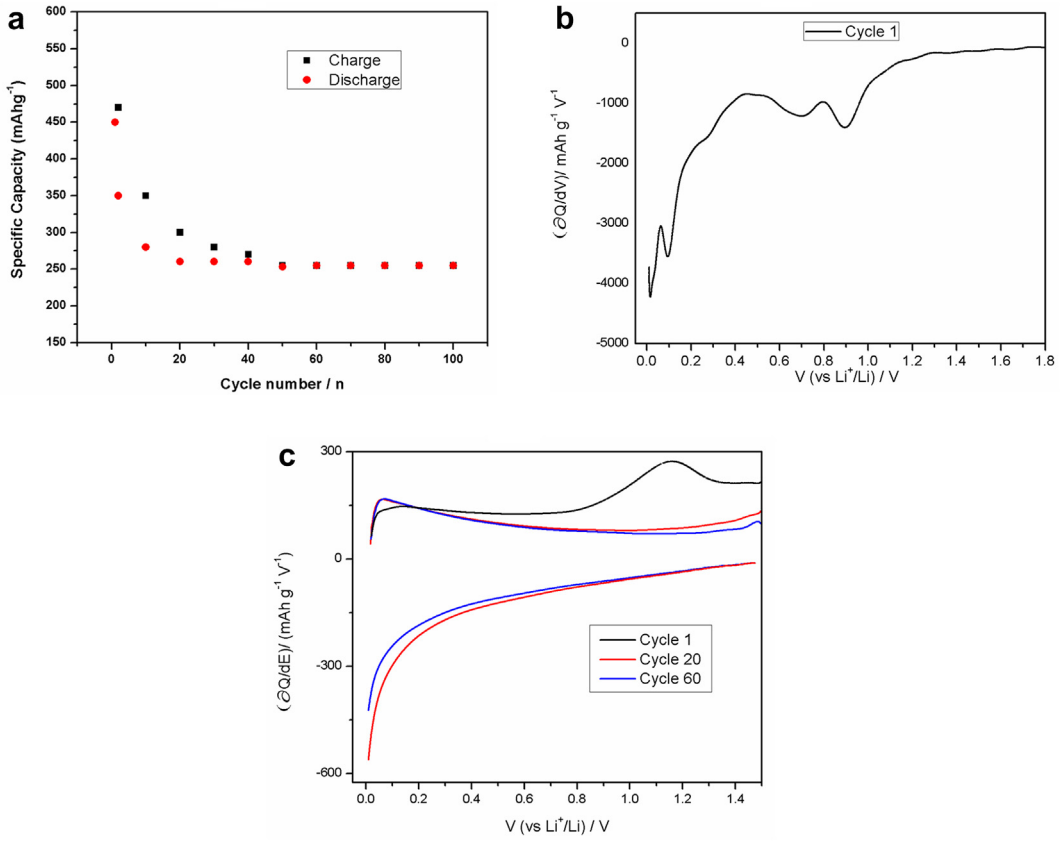

Fig. 3. a-) Specific capacity vs number of cycles for CMK-3 charged/discharged at 0.1 A g^{-1}. b-) Differential charge capacity vs potential of first cycle in CMK-3 charged at 0.1 A g^{-1}. c-) Differential charge/discharge capacity vs potential for the 1st, 20th and 60th cycles with CMK-3 charged at 0.1 A g^{-1}.

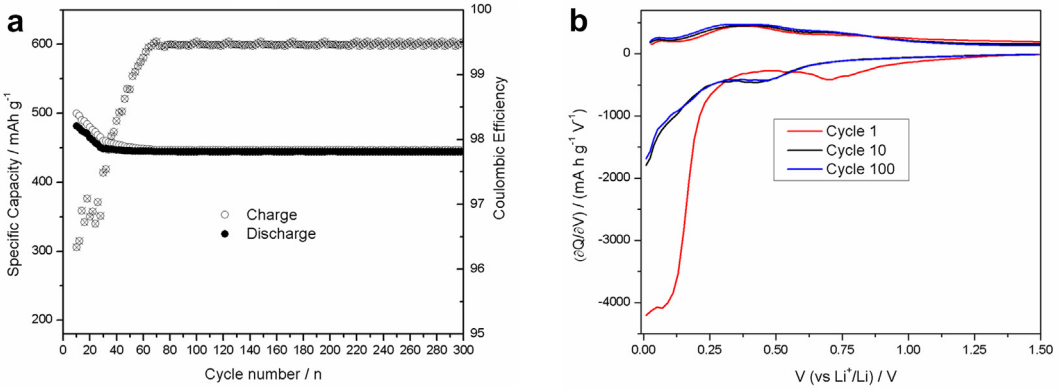

Fig. 4. a-) Specific capacity vs number of cycles for SBA-15/C charged/discharged at 0.1 A g^{-1}. b-) Differential charge/discharge capacity vs potential for 1st, 10th and 100th cycles with SBA-15/C charged at 0.1 A g^{-1}.

were taken: in one set of experiments, the electrodes were charged at a fixed current and discharged at different current regimes, whereas in the other set of experiments both the charge and the discharge were made at different current regimes, something that is less commonly found in the bibliography. In Fig. 6a, the working electrode was first charged and discharged at C/20 rate (first five points), and the remaining points were obtained by charging at C/5 and discharging at the different C-rates shown in the figure.

The charge/discharge experiments at C/20 showed that the material had a maximum capacity of 498 $mAhg^{-1}$, with the rate capability plot revealing that the increase in current density did not significantly alter the high specific capacity, which was then able to discharge in a short time. At the rate C/5, the discharge capacity was 460 $mAhg^{-1}$, decreasing to 390 mAh g^{-1} at a discharge rate of 4C. This indicates that SBA15/C could be discharged in 15 min, maintaining 78% of the capacity obtained at C/20. Then, when the current was set back to C/2, the electrode recovered the initial C/2 capacity.

It is also illustrative to estimate the intrinsic capacity of the silica material on the basis of the previous information. As stated above, the capacity found at the lowest charging/discharging rate was 498 mAh per gram of the SiO_2/C composite. If we attribute to the

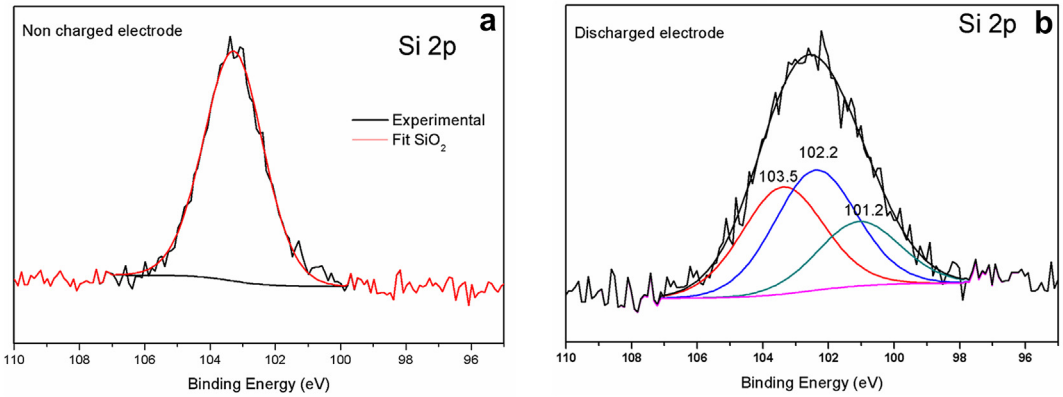

Fig. 5. a-) XPS spectrum of Si 2p for non-cycled SBA-15/C electrode (reference). b-) XPS spectrum of Si 2p for discharged SBA-15/C electrode after 30 cycles. The fit corresponds to a deconvolution assuming the presence of SiO_2 (103.5 eV), Si-C (101.2 eV) and lithium-silicate (102.2 eV) species.

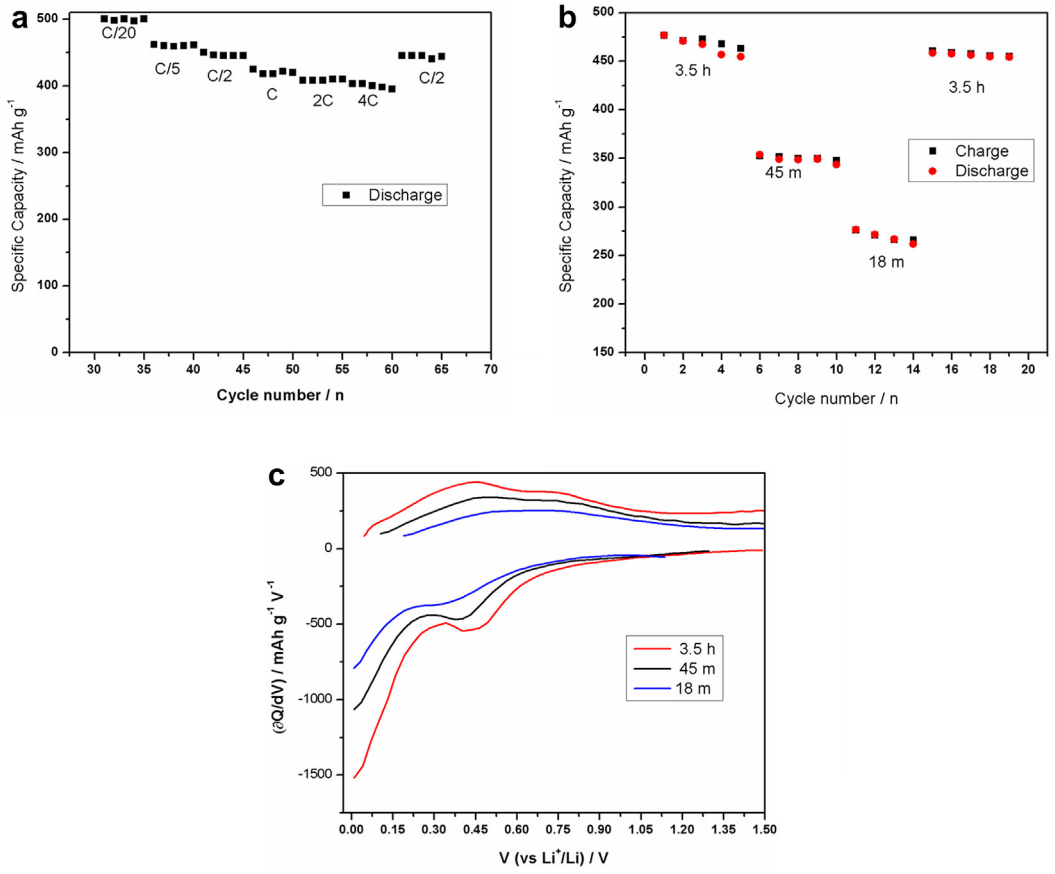

Fig. 6. a-) Rate capability of SBA-15/C. For the first five points charge/discharge was performed at C/20. The following points were obtained by charging at C/5 and discharging at the different rates indicated in the figure. b-) Rate capability of SBA-15/C. The charge/discharge was performed at the different rates indicated in the figure. c-) Differential charge/discharge capacity vs potential for SBA-15/C obtained at different rates of charge/discharge.

carbonaceous material a capacity of 250 $mAhg^{-1}$ (as can be inferred from the CMK3 results), and it is also taken into account that the carbon content of the composite is 45%, then this results in a capacity of 701 mAh per gram of the silica material, which is in good agreement with the prediction made above on the basis of the XPS results.

Fig. 6b displays the charge/discharge profile at different current regimes. It can be noted that at C/3.5 the capacity is 460 mAh g^{-1}. When the electrode was charged/discharged in one hour the capacity of charge and discharge decreased to 350 $mAhg^{-1}$, with the main accomplishment of this electrode being found at high current densities, where it is possible to obtain a the considerable charge/discharge capacity of 275 mAh g^{-1} in 18 min. Thus, it would be possible to charge an electrical device in a few minutes with a good specific capacity. Fig. 6c shows the dQ/dV plot of the electrode at different current regimes, where it can be seen that the different processes become less evident with increasing charge/discharge velocity. Nevertheless the peak potentials are only slightly altered

with respect to the values found at lower rates of charge/discharge.

Table 2 compares the present results of rate capability with other SiO_2/carbon materials proposed in the literature. Since the results were obtained under different conditions, we will use two figures of merit ($C_{\sim 1}$ and $C_{\sim 2}$) defined as:

$$C_{\sim 1} = \frac{\text{discharge capacity measured at the rate closest to 1C}}{\text{discharge capacity obtained at the lowest discharge rate}} \quad (5)$$

$$C_{\sim 4} = \frac{\text{discharge capacity measured at the rate closest to 4C}}{\text{discharge capacity at the lowest discharge rate}} \quad (6)$$

From this table, we can observe that at discharging rates close to 1C only one investigation reported in the literature presented results similar to ours. However, at rates close to 4C, the present composite seemed to show the best performance overall. Thus, the present SiO_2/C composite with the SBA-15/CMK-3 structure displays an excellent behavior in the discharging process at the high current discharging regime, showing a significant increase of power with respect to other related composites involving SiO_2/C structures.

4.5. Electrochemical impedance analysis

Having the CMK-3 structure in the SBA-15 matrix seems to allow a fast migration of ions and electrons towards SiO_2. The interconnected primary and secondary porous structure of CMK-3 allows a rapid reduction of the SiO_2 structure, and in addition, the highly ordered 3D structure of CMK-3 supports the volumetric and chemical changes of the SiO_2 structure and provides a more available and reversible lithium storage. To study the conductivity properties of the present composite, the EIS response was analyzed in the Nyquist and Bode plots, and equivalent circuits were fitted with different models, according to the discussion given in Supplementary Information.

Fig. 7a shows the Nyquist plot of the present silica/carbon composite before any electrochemical treatment and after 30 cycles. It can be seen that the resistance of the semicircle in the high frequency region decreased from 124 Ω to 36 Ω after the 30th charge/discharge cycles. The resulting reduction in resistance leads to an increase in conductivity after charging/discharging for 30 cycles, probably due to SEI and co-product formation. In fact, Li_2O, which presents a high conductivity of 2.10^3 $(\Omega\,cm)^{-1}$ [41], could appear through reaction R8, enhancing drastically the ionic conductivity, Fig. 7b shows the Nyquist plot of the electrode after 30 cycles at different states of charge. The resistance values of the semicircle at high frequencies were 36 Ω, 24 Ω and 20 Ω at 0%, 50% and 100% of charge, respectively, indicating an increase in the electrode conductivity, probably assisted by the carbon skeleton. On the other hand, a reversible high semicircle was observed at lower frequencies in the case of the fully charged electrode. This resistance may be attributed to a reversible reaction, which could be the formation of $Li_2Si_2O_5$, whose ionic conductivity is 4.5×10^{-9} $(\Omega\,cm)^{-1}$ [42], or to the reversible formation of a Li_xSi_y alloy, although this process has not yet been observed to date in Nyquist plots of similar systems in the literature [12,14,22,43,44].

As a general conclusion, it can be remarked that the large conductivity observed in the high frequency region of the impedance spectra was probably supported by the dense carbon skeleton and the SEI formed upon charging [12], which contributed significantly to the high performance observed in the charge/discharge process at high current regimes.

Table 2
Capacity retention for the SBA15/C composite of the present study compared with similar investigations using silica-containing composites reported in the literature. The figures of merit $C_{\sim 1}$ and $C_{\sim 2}$ are defined in the text. The values in parenthesis in the second column correspond to the rates closest to C in the corresponding study. The values in parenthesis in the third column correspond to rates closest to 4C in the corresponding study.

Reference	$C_{\sim 1}$	$C_{\sim 4}$
Jiao et al. [7]	0.61 (0.67C)	0.6 (2.67 C)
Li et al. [17]	0.81 (0.72 C)	0.50 (2.16 C)
H Tao et al. [18]	0.87 (0.72 C)	0.58 (4.34 C)
Z. Yuan et al. [42]	0.78 (1.25 C)	0.65 (5C)
J. Tu et al. [8]	0.79 (1C)	–
Li et al. [9]	0.69 (1.11 C)	–
P. Lv et al. [19]	0.80 (0.8 C)	–
Woo et al. [36]	0.75 (1C)	–
Ma et al. [20]	0.27 (1.33C)	0.14 (3.12 C)
Present investigation	0.88 (C)	0.79 (4 C)

4.6. Thermodynamic stability and potential of SiO_2lithiation

In a previous work, we calculated the free energy changes of reactions R1-R4, and showed that all these reactions are highly exothermic and exergonic at the reversible Li/Li^+ electrode potential. Thus, there is a very high probability that all these reactions occurred [9].

Using the above information and equation (2), we obtained the free energy for reactions R6-R9, involving the lithiation of SiO_2, as a function of the cell potential. This is shown in Fig. 8, where it can be observed that from 1.30 to 1.19 V reaction R6 is the most probable thermodynamically, since the formation of $Li_2Si_2O_5$ is the most exergonic reaction in this range of cell potentials. This reaction is already possible below 1.30 V, and the coexistence of the $Li_2Si_2O_5$/Li_2SiO_3 phases observed at 1.19 V. Li_2SiO_3 is the most stable phase in the narrow range between 1.19 V and 1.07 V. At 1.07 V, the coexistence of Li_2SiO_3/Li_4SiO_4 is observed, and Li_4SiO_4 becomes the most stable in the relatively wide potential range between 1.07 and 0.18 V. The coexistence of the Li_2O/Li_4SiO_4 phases is then observed at 0.2 V, and below this potential the formation of Li_2O becomes the most favored reaction. Although these calculations were made for crystalline phases and both, SiO_2 and Si are also known to occur in amorphous structures, we will see that they are useful for drawing qualitative conclusions. While the occurrence of amorphous SiO_2 would shift the calculated lines towards the left, the opposite would happen for the appearance of amorphous Si, so that these effects may eventually compensate.

At this point, it is interesting to analyze the previous information in the context of experimental results from the literature. We have superimposed in Fig. 8 information from the literature where the occurrence of the different phases analyzed here has been reported. There, we have drawn segments in the regions where different phases have been reported. We shortly discuss in the following paragraphs the sources of this information.

Using solid-state NRM, Kim et al. studied the Li^+ uptake/extraction mechanism in a SiO electrode, and proposed the formation of Li_4SiO_4 and Li_2O below 0.25 V [16,21], although the presence of Li_2SiO_3 and $Li_6Si_2O_7$ was not discarded. This corresponds to the first segment marked in Fig. 8. Furthermore, Sun et al. studied the insertion of Li in a SiO_2 thin film electrode, finding cathodic peaks at 1.0 and 0.77 V in the first cycle, which moved in the subsequent cycles to 1.54 and 0.87 V, respectively. These peaks were attributed to a two-step reaction of SiO_2 with lithium to produce $Li_2Si_2O_5$ and Si. This is represented in the plot as a bar below 1.15 V, which is the intermediate point between 0.87 V and 1.54 V [15].

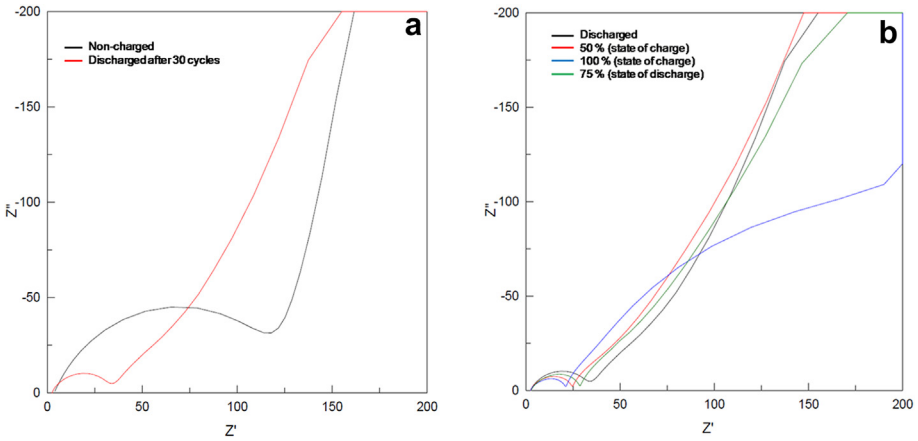

Fig. 7. a-) and b-) Nyquist plot of SBA-15/C at different states of charge.

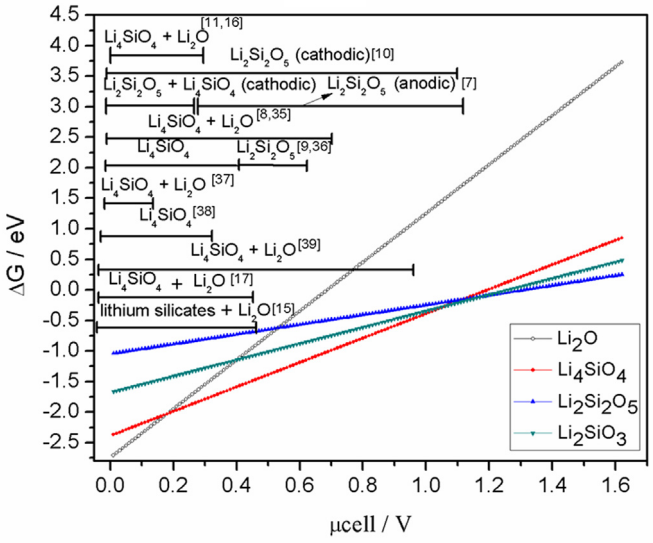

Fig. 8. Gibbs free energy of reaction calculated for the formation of different products stemming from the lithiation of SiO_2 according to reactions R6-R9, as a function of the cell potential. The segments in the inset denote the occurrence of different species at different potential ranges, according to results reported in the literature.

In another study, Jiao et al. [12] investigated SiO_2/carbon composite microspheres with a core-shell structure and found a cathodic peak at 0.28 V that was attributed to the reaction of SiO_2 with lithium ions, which formed $Li_2Si_2O_5$ and irreversible Li_4SiO_4, as well as an anodic peak at 1.2 V in all the oxidation cycles. This was found to be consistent with the reaction that turned $Li_2Si_2O_5$ reversibility into SiO_2. On the basis of this information, we have drawn a third row of segments in Fig. 8. Tu et al. [13,45] studied Li^+ storage in SiO_2 nanospheres and reported finding a voltammetric reduction peak at 0.72 V, which was attributed to SEI formation and Li_2O. This peak shifted to 0.68 V during periodic scans and $Li_4SiO_4$was detected in XPS experiments with charged electrodes, indicating the irreversible formation of these species. Thus, on the basis of this information, we have drawn a segment for Li_2O below approximately 0.7 V.

Li et al. [14,46] synthesized a sugar apple-shaped SiOx@C nanocomposite spheres and studied their lithiation behavior. Using selected area electron diffraction (SAED), these authors identified the crystalline $Li_2Si_2O_5$ phase below 0.6 V and also both the crystalline Li_2SiO_4 and Li_2O phases below 0.4 V, which are drawn with corresponding segments in Fig. 8. Yao et [47] al examined the behavior of carbon-coated SiO_2 nanoparticles as anode material for lithium ion batteries and attributed a cathodic voltammetric peak at 0.15 V to the formation of amorphous Li_2O or crystalline Li_4SiO_4. These results are illustrated as segments in the sixth row in Fig. 8.

In another investigation, Hao et al. [48] embedded amorphous silica uniformly at the nano-scale in the tunnel wall of mesoporous carbon, avoiding free or aggregated silica or carbon particles in the cavity of the tunnels. In the voltammetric profiles, three peaks were observed, with the one at 0.32 V being attributed to the reduction of SiO_2. On the other hand, FTIR spectroscopy indicated the existence of Li_4SiO_4. Thus, in Fig. 8, we have drawn a segment below 0.32 V, which suggests the existence of this phase at these potentials. In addition, Yuan et al. [49] synthesized a 3D porous carbon structure with amorphous SiO_2 nanoparticles embedded in the wall of the pores, and reported two reduction peaks at 1 and 0.5 V in the first cycle. The second of these peaks was attributed to electrolyte decomposition and the formation of a solid electrolyte interphase layer. Since these authors then stated that the initial irreversible capacity was partly due to the formation of a solid electrolyte interphase film on the electrode surface, resulting in the irreversible formation of Li_2O and Li_4SiO_4, we have included in Fig. 8 a segment with these two species below 1 V.

Li et al. [22] synthesized spherical SiO_2/C nano-composites with a dual porosity, of 2.17 and 2.85 nm pore diameters. XPS spectroscopy was used to analyze the composition of the products at different states of charges, and a reduction peak located around 0.75 V was found in the first cycle, which became indiscernible in the subsequent cycles and was attributed to SEI formation. In addition, two cathodic peaks at 0.45 V and 0.2 V in the further cycles were assigned to the formation of Li_2O and Li_4SiO_4. These results are plotted in the corresponding segment in the ninth row of Fig. 8. Finally, Kim et al. [20] prepared a SiO_2-carbon composite obtained by chelation of silicon with citric acid in a glyme-based solvent. The irreversible generation of Li_2O and lithium silicates by the lithiation of SiO_2, as well as by the irreversible formation of solid electrolyte interphase (SEI) layer, was related to a small cathodic peak at 0.53 V in the initial charging. This is schematized by the corresponding segment at the tenth row of Fig. 8.

Although it is not possible to draw straightforward conclusions from the above data, as a general rule it can be stated that Li_2O and Li_4SiO_4 occur at the lower potentials whereas at higher potentials the compound most often found is $Li_2Si_2O_5$. The silicate Li_2SiO_3 was only mentioned in one of the articles [16] and as an impurity. All the

Table 3
Estimation of the amount of charge stored as reversible silicates (Q_{SiO}) and as Si-Li alloy ($Q_{Si/C}$) in the present composite material. Columns 3 and 4 give the relative amounts.

Charging time	Q_{SiO}/mAh g^{-1}	$Q_{Si/C}$/mAh g^{-1}	$Q_{SiO}/(Q_{SiO} + Q_{Si/C})$	$Q_{Si/C}/(Q_{SiO} + Q_{Si/C})$
3.5 h	174	306	0.36	0.64
45 min	161	190	0.46	0.54
18 min	131	130	0.50	0.50

The term $Q_{Si/C}$ includes the charge due to the Li^+ storage in the carbon skeleton.

above findings roughly reflect the predictions drawn by first-principles calculations, where the occurrence of different species with increasing potential is given by $Li_2O \rightarrow Li_4SiO_4 \rightarrow Li_2SiO_3 \rightarrow Li_2Si_2O_5$. The narrow stability range predicted for Li_2SiO_3 is in line with the fact that this species is seldom found. Another conclusion that may be drawn from the comparison between theory and experiment is that the occurrence of different species is actually predicted at a wider potential range than occurred in the experiments. This may be in part due to the fact that our analysis is mainly based on cathodic current peaks. Furthermore, kinetic limitations may explain the occurrence of different species at potentials lower than those expected from theoretical considerations.

4.7. Contributions to the reversible storage capacity

On the basis of the previous analysis, the calculation of the theoretical charge/discharge capacity of SiO_2 is complicated due to the occurrence of different possible reactions, which yield various products with different compositions depending on the specific kinetics of each reaction. According to the literature reporting on similar systems, the nature of reactions R6-R9 can be separated into reversible and irreversible reactions, and once the irreversible reactions occur in the early cycles the reversible reactions occur in the subsequent cycles [14,16].

For the present composites, the differential charge/discharge plots versus the potential for SiO_2/C composite (Fig. 4b) shows two regions of reversible charge storage, with one being around 0.43 V and other below 0.2 V. Based on the discussion above, we can assign the reversible lithium insertion at lower potentials to the formation of the Li_xSi_y alloy and to the lithium storage in carbonaceous skeleton. At higher potentials, the lithiation should lead to the reversible formation of some silicate species, with these processes becoming evident after the early cycling of the electrodes.

In order to analyze the different kinetic natures of the reactions taking place at large and low potentials, we now address the results shown in Fig. 6c, where the $\frac{\partial Q}{\partial V}$ plots are shown at different C rates. The two regions in the charging profiles can be separated into one at lower potentials involving a monotonic increase (in the absolute value) of $\frac{\partial Q}{\partial V}$, and another one at larger potentials, where $\frac{\partial Q}{\partial V}$ indicates a peak or a shoulder. To separate these two regions, we chose the potential values V_{conc} of 0.37 V, 0.29 V and 0.26 V for the charging times of 3.5 h, 45 min and 18 min, respectively, which correspond to the potentials where the negative $\frac{\partial Q}{\partial V}$ plots show the maximum concavity. Table 3 gives the amount of charge stored at $V > V_{conc}$ and $V < V_{conc}$, which we denote by Q_{SiO} and $Q_{Si/C}$, respectively, since we expect that these values will give the amount of Li^+ charge stored as silicates or in Si alloys. The latter is also expected to contain the contribution of Li^+ storage in the carbonaceous skeleton. It can be observed that as the charging rate increases, the amount of charge stored in the reversible silicate Q_{SiO} slightly decreases. However, its relative contribution $Q_{SiO}/(Q_{SiO} + Q_{Si/C})$ increases, indicating that the other Li^+ storage processes are relative slower.

5. Conclusions

In the present work, we propose a material as an anode with facile synthesis, which can be charged/discharged at high current densities, while maintaining a very good specific capacity. Moreover, the lithium silicates and silicon formed during the electrochemical reduction process can be effectively trapped in a stable carbon template and in the lithium oxide/silicates, thereby protecting the electrode from the direct contact with the electrolyte and increasing the cyclability, while preserving the capacity at high current regimes [22,40,50–52].

A better synergetic effect was observed in the SBA-15/C composite in comparison with separate SBA-15 and CMK-3 materials, with the combination between the specific capacity of SiO_2 with the conductivity of CMK-3 permitting reversible lithium storage. The resulting composite showed not only a high cyclability and the ability to maintain a high capacity even at elevated current densities, but also allowed a fast charge/discharge in 18 min while preserving an excellent capacity. This composite could be applicable for both stationary and mobile uses.

Acknowledgments

This work was supported by PIO Conicet-YPF 3855/15, PID Conicet-11220110100992, PID Conicet-11220150100624, Program BID-Foncyt (PICT-2012-2324, PICT-2015-1605), SeCyT of the Universidad Nacional de Córdoba and YPF-Tecnología (Y-TEC), Argentina. This work was performed at INFIQC-IFEG-CONICET and Facultad de CienciasQuímicas, FaMAF. Universidad Nacional de Córdoba, Argentina. This work used the Mendieta Cluster from CCAD-UNC, which is a part of SNCAD-MinCyT, Argentina. An IPAC grant from SNCAD-MinCyT, Argentina is also acknowledged. The authors wish to acknowledge the helpful to obtain the STEM-EDS micrograph of Dr. Alberto Caneiro and Dr. Melina Cozzarini.

Appendix A. Supplementary data

Supplementary data related to this article can be found at https://doi.org/10.1016/j.electacta.2018.05.050.

References

[1] S. Bourderau, T. Brousse, D. Schleich, Amorphous silicon as a possible anode material for Li-ion batteries, J. Power Sources. 81–82 (1999) 233–236, https://doi.org/10.1016/S0378-7753(99)00194-9.
[2] M.N. Obrovac, V.L. Chevrier, Alloy negative electrodes for Li-ion batteries, Chem. Rev. 114 (2014) 11444–11502, https://doi.org/10.1021/cr500207g.
[3] B. Liang, Y. Liu, Y. Xu, Silicon-based materials as high capacity anodes for next generation lithium ion batteries, J. Power Sources. 267 (2014) 469–490, https://doi.org/10.1016/j.jpowsour.2014.05.096.
[4] K. Feng, M. Li, W. Liu, A.G. Kashkooli, X. Xiao, M. Cai, Z. Chen, Silicon-based anodes for lithium-ion batteries: from fundamentals to practical applications, Small 14 (2018), https://doi.org/10.1002/smll.201702737.
[5] X. Su, Q. Wu, J. Li, X. Xiao, A. Lott, W. Lu, B.W. Sheldon, J. Wu, Silicon-based nanomaterials for lithium-ion batteries: a review, Adv. Energy Mater. 4 (2013) 1–23, https://doi.org/10.1002/aenm.201300882.
[6] M.L. Terranova, S. Orlanducci, E. Tamburri, V. Guglielmotti, M. Rossi, Si/C hybrid nanostructures for Li-ion anodes: an overview, J. Power Sources. 246 (2014) 167–177, https://doi.org/10.1016/j.jpowsour.2013.07.065.
[7] H. Jia, P. Gao, J. Yang, J. Wang, Y. Nuli, Z. Yang, Novel three-dimensional mesoporous silicon for high power lithium-ion battery anode material, Adv. Energy Mater. 1 (2011) 1036–1039, https://doi.org/10.1002/aenm.201100485.
[8] X. Xin, X. Zhou, F. Wang, X. Yao, X. Xu, Y. Zhu, Z. Liu, A 3D porous architecture of Si/graphene nanocomposite as high-performance anode materials for Li-ion

batteries, J. Mater. Chem. 22 (2012) 7724, https://doi.org/10.1039/c2jm00120a.
[9] G. Lener, M. Otero, D.E. Barraco, E.P.M. Leiva, Energetics of silica lithiation and its applications to lithium ion batteries, Electrochim. Acta 259 (2018) 1053–1058, https://doi.org/10.1016/j.electacta.2017.10.126.
[10] R. Dash, S. Pannala, Theoretical limits of energy density in silicon-carbon composite anode based lithium ion batteries, Sci. Rep. 6 (2016) 27449, https://doi.org/10.1038/srep27449.
[11] M.N. Obrovac, L. Christensen, Structural changes in silicon anodes during lithium insertion/extraction, Electrochem. Solid state Lett. 7 (2004) A93–A96, https://doi.org/10.1149/1.1652421.
[12] M. Jiao, K. Liu, Z. Shi, C. Wang, SiO $_2$/carbon composite microspheres with hollow core-shell structure as a high-stability electrode for lithium-ion batteries, ChemElectroChem 4 (2017) 542–549, https://doi.org/10.1002/celc.201600658.
[13] J. Tu, Y. Yuan, P. Zhan, H. Jiao, X. Wang, H. Zhu, S. Jiao, Straightforward approach toward SiO 2 nanospheres and their superior lithium storage performance, J. Phys. Chem. C 118 (2014) 7357–7362, https://doi.org/10.1021/jp5011023.
[14] M. Li, Y. Zeng, Y. Ren, C. Zeng, J. Gu, X. Feng, H. He, Fabrication and lithium storage performance of sugar apple-shaped SiOx@C nanocomposite spheres, J. Power Sources. 288 (2015) 53–61, https://doi.org/10.1016/j.jpowsour.2015.04.127.
[15] Q. Sun, B. Zhang, Z.-W. Fu, Lithium electrochemistry of SiO2 thin film electrode for lithium-ion batteries, Appl. Surf. Sci. 254 (2008) 3774–3779, https://doi.org/10.1016/j.apsusc.2007.11.058.
[16] T. Kim, S. Park, S.M. Oh, Solid-state NMR and electrochemical dilatometry study on Li+ uptake/extraction mechanism in SiO electrode, J. Electrochem. Soc. 154 (2007) A1112, https://doi.org/10.1149/1.2790282.
[17] M. a. Al-Maghrabi, J. Suzuki, R.J. Sanderson, V.L. Chevrier, R. a. Dunlap, J.R. Dahn, Combinatorial studies of Si1−xOx as a potential negative electrode material for Li-Ion battery applications, J. Electrochem. Soc. 160 (2013) A1587–A1593, https://doi.org/10.1149/2.115309jes.
[18] C.C. Nguyen, H. Choi, S.-W. Song, Roles of oxygen and interfacial stabilization in enhancing the cycling ability of silicon oxide anodes for rechargeable lithium batteries, J. Electrochem. Soc. 160 (2013) A906–A914, https://doi.org/10.1149/2.118306jes.
[19] M. Oschatz, J.T. Lee, H. Kim, W. Nickel, L. Borchardt, W.I. Cho, C. Ziegler, S. Kaskel, G. Yushin, Micro- and mesoporous carbide-derived carbon prepared by a sacrificial template method in high performance lithium sulfur battery cathodes, J. Mater. Chem. A. 2 (2014) 17649–17654, https://doi.org/10.1039/C4TA03327B.
[20] J.Y. Kim, D.T. Nguyen, J.S. Kang, S.W. Song, Facile synthesis and stable cycling ability of hollow submicron silicon oxide-carbon composite anode material for Li-ion battery, J. Alloys Compd. 633 (2015) 92–96, https://doi.org/10.1016/j.jallcom.2015.01.309.
[21] B. Guo, J. Shu, Z. Wang, H. Yang, L. Shi, Y. Liu, L. Chen, Electrochemical reduction of nano-SiO2 in hard carbon as anode material for lithium ion batteries, Electrochem. Commun. 10 (2008) 1876–1878, https://doi.org/10.1016/j.elecom.2008.09.032.
[22] H.H. Li, X.L. Wu, H.Z. Sun, K. Wang, C.Y. Fan, L.L. Zhang, F.M. Yang, J.P. Zhang, Dual-Porosity SiO2/C nanocomposite with enhanced lithium storage performance, J. Phys. Chem. C 119 (2015) 3495–3501, https://doi.org/10.1021/jp511435w.
[23] H.-C. Tao, L.-Z. Fan, X. Qu, Facile synthesis of ordered porous Si@C nanorods as anode materials for Li-ion batteries, Electrochim. Acta 71 (2012) 194–200, https://doi.org/10.1016/j.electacta.2012.03.139.
[24] P. Lv, H. Zhao, J. Wang, X. Liu, T. Zhang, Q. Xia, Facile preparation and electrochemical properties of amorphous SiO2/C composite as anode material for lithium ion batteries, J. Power Sources. 237 (2013) 291–294, https://doi.org/10.1016/j.jpowsour.2013.03.054.
[25] X. Ma, Z. Wei, H. Han, X. Wang, K. Cui, L. Yang, Tunable construction of multi-shell hollow SiO2 microspheres with hierarchically porous structure as high-performance anodes for lithium-ion batteries, Chem. Eng. J. 323 (2017) 252–259, https://doi.org/10.1016/j.cej.2017.04.108.
[26] H. Zhou, S. Zhu, M. Hibino, I. Honma, Electrochemical capacitance of self-ordered mesoporous carbon, J. Power Sources 122 (2003) 219–223, https://doi.org/10.1016/S0378-7753(03)00439-7.
[27] D. Zhao, Triblock copolymer syntheses of mesoporous silica with periodic 50 to300 angstrom pores, Science (80-.) 279 (1998) 548–552, https://doi.org/10.1126/science.279.5350.548.
[28] D. Zhao, Q. Huo, J. Feng, B.F. Chmelka, G.D. Stucky, Nonionic triblock and star diblock copolymer and oligomeric surfactant syntheses of highly ordered, hydrothermally stable, mesoporous silica structures, J. Am. Chem. Soc. 120 (1998) 6024–6036, https://doi.org/10.1021/ja974025i.
[29] P. Janus, R. Janus, P. Kuśtrowski, S. Jarczewski, A. Wach, A.M. Silvestre-Albero, F. Rodríguez-Reinoso, Chemically activated poly(furfuryl alcohol)-derived CMK-3 carbon catalysts for the oxidative dehydrogenation of ethylbenzene, Catal. Today 235 (2014) 201–209, https://doi.org/10.1016/j.cattod.2014.03.019.
[30] A.M. Wilson, J.N. Reimers, E.W. Fuller, J.R. Dahn, Lithium insertion in pyrolyzed siloxane polymers, Solid State Ionics 74 (1994) 249–254, https://doi.org/10.1016/0167-2738(94)90217-8.
[31] P.I. Ravikovitch, A.V. Neimark, Characterization of micro- and mesoporosity in SBA-15 materials from adsorption data by the NLDFT method, J. Phys. Chem. B 105 (2001) 6817–6823, https://doi.org/10.1021/jp010621u.
[32] M. Kruk, M. Jaroniec, C.H. Ko, R. Ryoo, Characterization of the porous structure of SBA-15, Chem. Mater. 12 (2000) 1961–1968, https://doi.org/10.1021/cm000164e.
[33] P. Giannozzi, S. Baroni, N. Bonini, M. Calandra, R. Car, C. Cavazzoni, D. Ceresoli, G.L. Chiarotti, m. Cococcioni, I. Dabo, A.D. Corso, S. Fabris, G. Fratesi, S. de Gironcoli, R. Gebauer, U. Gerstmann, C. Gougoussis, A. Kokalj, M. Lazzeri, L. Martin-Samos, N. Marzari, F. Mauri, R. Mazzarello, S. Paolini, A. Pasquarello, L. Paulatto, C. Sbraccia, S. Scandolo, G. Sclauzero, A.P. Seitsonen, A. Smogunov, P. Umari, R.M. Wentzcovitch, Quantum ESPRESSO: a Modular and Open-source Software Project for Quantum Simulations of Materials, 2009, https://doi.org/10.1088/0953-8984/21/39/395502.
[34] L.A. Cano, A.A. Garcia Blanco, G. Lener, S.G. Marchetti, K. Sapag, Effect of the support and promoters in Fischer-Tropsch synthesis using supported Fe catalysts, Catal. Today (2016), https://doi.org/10.1016/j.cattod.2016.06.054.
[35] H. Zhou, S. Zhu, M. Hibino, I. Honma, M. Ichihara, Lithium storage in ordered mesoporous carbon (CMK-3) with high reversible specific energy capacity and good cycling performance, Adv. Mater. 15 (2003) 2107–2111, https://doi.org/10.1002/adma.200306125.
[36] D. Saikia, T.-H. Wang, C.-J. Chou, J. Fang, L.-D. Tsai, H.-M. Kao, A comparative study of ordered mesoporous carbons with different pore structures as anode materials for lithium-ion batteries, RSC Adv. 5 (2015) 42922–42930, https://doi.org/10.1039/c5ra05168a.
[37] R. Guo, L. Zhao, W. Yue, Assembly of core-shell structured porous carbon-graphene composites as anode materials for lithium-ion batteries, Electrochim. Acta 152 (2015) 338–344, https://doi.org/10.1016/j.electacta.2014.11.140.
[38] D.-W. Wang, F. Li, M. Liu, G.Q. Lu, H.-M. Cheng, 3D aperiodic hierarchical porous graphitic carbon for high rate - suporting informaton, Angew. Chem. 47 (2008) 373–376, https://doi.org/10.1002/anie.200702721.
[39] L. a. Solovyov, a. N. Shmakov, V.I. Zaikovskii, S.H. Joo, R. Ryoo, Detailed structure of the hexagonally packed mesostructured carbon material CMK-3, Carbon N. Y 40 (2002) 2477–2481, https://doi.org/10.1016/S0008-6223(02)00160-4.
[40] T.D. Bogart, D. Oka, X. Lu, M. Gu, C. Wang, B.A. Korgel, Lithium ion battery performance of silicon nanowires with carbon skin, ACS Nano 8 (2014) 915–922, https://doi.org/10.1021/nn405710w.
[41] P. Heitjans, S. Indris, Diffusion and ionic conduction in nanocrystalline ceramics, J. Phys. Condens. Matter 15 (2003) R1257–R1289, https://doi.org/10.1088/0953-8984/15/30/202.
[42] I.D. Raistrick, Ionic conductivity of some lithium silicates and aluminosilicates, J. Electrochem. Soc. 123 (1976) 1469, https://doi.org/10.1149/1.2132621.
[43] J. Woo, S.-H. Baek, A comparative investigation of different chemical treatments on SiO anode materials for lithium-ion batteries: towards long-term stability, RSC Adv. 7 (2017) 4501–4509, https://doi.org/10.1039/C6RA27804C.
[44] Y. Ru, D.G. Evans, H. Zhu, W. Yang, Facile fabrication of yolk-shell structured porous Si-C microspheres as effective anode materials for Li-ion batteries, RSC Adv. 4 (2014) 71–75, https://doi.org/10.1039/C3RA44752A.
[45] D. Mazouzi, B. Lestriez, L. Roué, D. Guyomard, Silicon composite electrode with high capacity and long cycle life, Electrochem. Solid state Lett. 12 (2009) A215, https://doi.org/10.1149/1.3212894.
[46] J.S. Bridel, T. Azaïs, M. Morcrette, J.M. Tarascon, D. Larcher, Key parameters governing the reversibility of Si/carbon/CMC electrodes for Li-ion batteries, Chem. Mater. 22 (2010) 1229–1241, https://doi.org/10.1021/cm902688w.
[47] Y. Yao, J. Zhang, L. Xue, T. Huang, A. Yu, Carbon-coated SiO2 nanoparticles as anode material for lithium ion batteries, J. Power Sources. 196 (2011) 10240–10243, https://doi.org/10.1016/j.jpowsour.2011.08.009.
[48] S. Hao, Z. Wang, L. Chen, Amorphous SiO2 in tunnel-structured mesoporous carbon and its anode performance in Li-ion batteries, Mater. Des. 111 (2016) 616–621, https://doi.org/10.1016/j.matdes.2016.09.020.
[49] Z. Yuan, N. Zhao, C. Shi, E. Liu, C. He, F. He, Synthesis of SiO2/3D porous carbon composite as anode material with enhanced lithium storage performance, Chem. Phys. Lett. 651 (2016) 19–23, https://doi.org/10.1016/j.cplett.2016.03.015.
[50] Q. Sun, B. Zhang, Z.W. Fu, Lithium electrochemistry of SiO2 thin film electrode for lithium-ion batteries, Appl. Surf. Sci. 254 (2008) 3774–3779, https://doi.org/10.1016/j.apsusc.2007.11.058.
[51] J. Wang, H. Zhao, J. He, C. Wang, J. Wang, Nano-sized SiOx/C composite anode for lithium ion batteries, J. Power Sources. 196 (2011) 4811–4815, https://doi.org/10.1016/j.jpowsour.2011.01.053.
[52] M. Yoshio, H. Wang, K. Fukuda, T. Umeno, N. Dimov, Z. Ogumi, Carbon-coated Si as a lithium-ion battery anode material, J. Electrochem. Soc. 149 (2002) A1598, https://doi.org/10.1149/1.1518988.